JOURNAL OF MATERIALS SCIENCE 32 (1997) 5467–5475

# Damage and failure behaviour of a woven C/SiC material

L. HAHN, F. ANSORGE, A. BRÜCKNER-FOIT
*Institut für Zuverlässigkeit und Schadenskunde im Maschinenbau, Universität Karlsruhe, Postfach 36 40, D-76021 Karlsruhe, Germany*

The mechanical behaviour of a C/SiC material, infiltrated by liquid silicon, was investigated. Structural features have been attributed to the damage and failure behaviour of the material. The material can be described by a two-component model: the fibre bundles in the loading direction (component 1), and the rest of structure (component 2). The fibre bundles in the loading direction largely determine the deformation and failure behaviour, whereas the rest of the structure essentially determines the damage behaviour of the material. The structural features do not undergo changes up to 1400 °C in mechanical tests, whereas the mechanical properties undergo slight changes. Heat treatment of the material at elevated temperatures causes a change in the structural features and leads to a reduction in strength and in interlaminar shear strength.

## 1. Introduction

The damage tolerance of ceramic materials can be enhanced by embedding high-strength carbon or silicon carbide fibres. In recent years, a multitude of different fibre–matrix combinations have been developed. Depending on the configuration of fibre, matrix and interface connecting the fibres with the matrix, the fracture mechanism undergoes decisive changes. Carbon fibre-reinforced materials provided with a protective oxide layer are suitable candidates in high-temperature application. Materials with matrices made of SiC, using the liquid siliconization technique [1], can be produced at reasonable cost. Complete infiltration with silicon is feasible solely with woven fibre-reinforced materials.

This study aimed to gain an understanding of the mechanical behaviour of liquid siliconized 0°/90° carbon-fibre fabric–silicon carbide matrix composites (C/SiC) under various loading and temperature conditions.

No description can be found in the literature of the behaviour of 0°/90° carbon-fibre fabric–silicon carbide matrix composites (C/SiC). Investigations of the behaviour of other fabrics help to improve knowledge of this material.

Typical stress–strain plots (σ–ε plots) of fibre-reinforced SiC/SiC have their origins in a clearly linear zone and undergo more or less kinking before attainment of the ultimate load [2, 3]. In terms of phenomenology, the linear range of origin is considered to be linear-elastic, in analogy with the unidirectional composites. Rouby and Reynaud [4] and Shuler *et al.* [5] attributed the next range to progressive damage of the matrix, which occurs in parallel with the onset of damage to the fibre. Fibres fail by bundles and the specimen exhibits smooth fracture areas [6]. Rouby and Reynaud [4] supposed that the matrix material, in accordance with the ACK model [7], will break under load into equidistant fragments. The cracks are bridged by the fibres. Depending on the stress applied, the fraction of broken fibres is determined. This increases to a critical value which is equivalent to the maximum stress tolerated by the bridged crack. Reynaud [8] described the failure at maximum stress by reference to modified weakest link statistics.

The loading/unloading behaviour depends crucially on the fibre/matrix configuration [2]. In analogy with unidirectional materials, SiC/SiC and C/C composites first exhibit linear-elastic behaviour without permanent deformation. At higher stress levels, the irreversible deformation and the hysteresis area increase continuously until fracture of the specimens. Plies in a 90° orientation are passed by a crack along the fibres which do not produce damage in the fibre. In plies in the 0° direction, a damage zone develops whose size depends on microstructural parameters such as interface bonding and strength of fibres and matrix. The irreversible deformation is attributed to the friction between matrix fragments and the fibres. Depending on the respective load applied, this gives rise to differing Young's moduli and hence to a hysteresis curve.

There have been very few experiments performed at high temperatures, or experiments involving specimens heat treated at elevated temperature. It appears that materials with a matrix made of glass ceramics lose their strength with increasing temperature, provided that the experiments are carried out in air [9]. This is an effect of oxidation. High-temperature experiments conducted in argon ($T_{max} = 1300\,°C$) do not lead to changes in strength [9]. Mahfuz *et al.* [10] observed an increase in the

0022–2461  

Young's modulus and in the flexural strength with tests on woven material with coated fibre-reinforced C/C specimens. No statements were made regarding fracture mechanisms. It is assumed that there are low residual stresses at elevated temperatures because higher temperatures are close to the manufacturing temperature.

Sbaizero *et al.* [11] described the crack propagation behaviour in the 90° plies of a laminated composite. They investigated SiC fibre-reinforced glass ceramics. The initiation of crack growth depended on the resistance to fracture of the matrix and of the interface of the 0° and 90° plies. If it was too low, propagation of delamination cracks always occurred along the 0° plies which cannot be penetrated by the crack.

A great number of publications are available on the theoretical description of the damage and failure mechanism of the fibre-reinforced composites. Evans *et al.* [12, 13] developed a model describing glassy or glass ceramic matrices having small pore volumes. Beyerle *et al.* [14] extended the model to include laminated SiC/CAS and indicated fracture mechanics approaches to calculating the failure behaviour.

Inghels and Lamon [15] also proposed a model for C/SiC and SiC/SiC, which is based on an initially undamaged fibre and matrix. This model was built from the relations derived by Evans and Marshall [12] and extended by Inghels and Lamon [15]. Wang *et al.* [16] and Shuler *et al.* [5] presented solely phenomenological descriptions of damage and crack propagation.

Another model, which can be applied to fibre-reinforced composites, has been described by Dinkler *et al.* [17] who proposed a material law based on the classical formulation of a homogeneous material with anisotropic elastic and plastic properties. Wang *et al.* [18] dealt with a model for laminated composites in which the 0° plies (fibres running parallel to the load), following failure of the 90° plies, are approximated by a number of springs. The latter springs are attributed the respective elastic properties. Using this model, the critical strain for the onset and propagation of transverse cracks as well as load versus displacement diagrams, can be calculated.

Pleitner and Kossira [19] proposed a self-contained description of the mechanical behaviour of fibre-reinforced ceramics. The basic stress–strain relations in this model are derived using a unit cell which contains a typical fibre/matrix configuration. These relations are then used to calculate the response of a system of coupled springs and friction elements. A layered beam element results in the 0° and the 90° plies, respectively, within the framework of a finite element analysis of a test specimen or a component.

The purpose of this work was to study the mechanical behaviour of a woven C/SiC material and to relate the phenomena observed to microstructural features. In the four-point bending test, the deformation behaviour of the material and its strength were determined. Loading/unloading experiments allowed statements to be made on irreversible deformations. The hystereses provided information about damage mechanisms which are effective in the material, whilst shear experiments have furnished data regarding interlaminar shear strength.

The mechanical behaviour was tested at room temperature on specimens in the condition as-received from the supplier, as well as on specimens subjected to thermal treatment in a vacuum. Further mechanical tests in the vacuum were performed at test temperatures from 1000–1400 °C.

The mechanical tests were followed by microstructural investigations in all cases, in order to determine the respective changes in the microstructure.

## 2. Experimental procedure

### 2.1. Material

The investigations were performed on a two-dimensional woven carbon-fibre fibre-reinforced SiC material (C/SiC) received from DLR Stuttgart [20, 21]. The material had been manufactured by the liquid siliconization technique. The following process steps were involved: the carbon-fibre fabric was embedded into a precursor resin with high carbon content and carbonized at 800 °C. Then it was subjected to siliconization at 1600 °C. During the process, carbon reacts with silicon to become SiC. During the cooling step, many cracks are produced. So it can be assumed that there are low residual stresses at room temperature because of these cracks.

A micrograph of the material is shown in Fig. 1. The fabric structure is made of fibre plies running in the direction of loading (the 0° fibre plies) and the fibre plies running normal to the direction of loading (the 90° fibre plies). The macroscopically visible fibre bundles of the individual layers of fabric have been segmented into approximately 200 μm wide sub-bundles. The individual fibre bundles are separated by a layer consisting of SiC matrix. The structure contains pores and cracks of various shapes and sizes.

Each sub-bundle is enclosed by a 10–60 μm thick SiC layer consisting of fine- and coarse-grained silicon carbide. The mean grain size of the fine-grained SiC is about 0.5 μm. It was produced by a reaction of silicon with the carbon fibres. The grain size of coarse-grained SiC is about 5 μm. Within one sub-bundle only the carbon matrix is present, with the

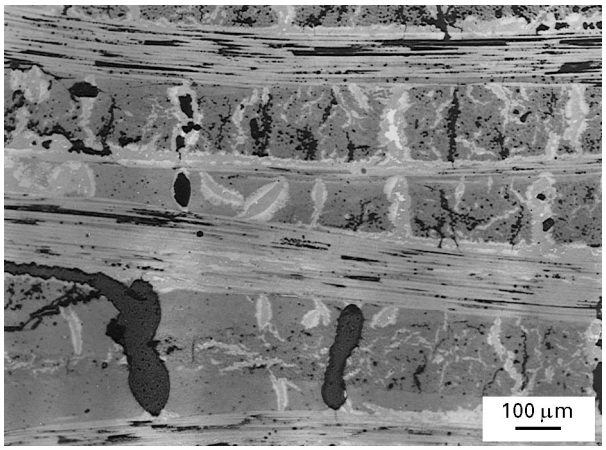


*Figure 1* Structure of an untreated specimen.

fibres embedded in it. The fibres are embedded in the matrix without visible interphase.

A distinction is made between three types of defect populations: the shrinkage cracks between the fibre sub-bundles and the cracks and pores within the SiC matrix. The shrinkage cracks occur one or two times per sub-bundle with about 50–150 μm spacing. SiC matrix cracks are present approximately equidistantly everywhere in the SiC matrix layers between the sub-bundles. The pores are not uniformly distributed, but accumulate as macropores, predominantly in the centre of the plate.

Each SiC matrix crack runs as an annulus around a sub-bundle and ends in at least one shrinkage crack. The SiC matrix layer is not a through-the-thickness layer, but surrounds the carbon fibre bundles as individual segments. Likewise, the shrinking cracks are not through-the-thickness cracks. It has rather been observed on depth microsections that individual fibres migrate from one side of the bundle to the other, thus bridging the crack.

## 2.2 Four-point bending test

The deformation behaviour and the strengths of the specimens were recorded in the four-point bending test with monotonic load applied. Irreversible effects were studied in loading/unloading experiments. Crack propagation was examined on notched specimens ($a/W = 0.25$).

Fixtures with an outer distance of 40 mm and an inner distance of the fixtures of 20 mm were used. The deflection was measured with an inductive strain transducer.

The strength experiments were displacement-controlled and carried out at a loading rate of 5 mm min$^{-1}$. Five specimens each were examined, with the mean value and the standard deviation of strength calculated from them. The σ–ε diagram plotted corresponds to one characteristic specimen.

In loading/unloading experiments, a sinus-shaped ramp of 1 mm min$^{-1}$ with displacement control was used.

## 2.3. Shear tests

The interlaminar shear strength was determined in a slant shear test involving untreated and heat-treated specimens. The apparatus for the slant shear test, according to Kadotani and Aki [22], is represented schematically in Fig. 2. In this test equipment, normal compressive stresses are superimposed on the shear stresses by variation of the angle, and their influence on the failure behaviour is studied.

The applied load can be represented in the triangle of forces as the tangential force superimposed on the normal force. The following relations hold

$$\tau = \frac{F \cos \alpha}{l\, b} \tag{1a}$$

$$\sigma = \frac{F \sin \alpha}{l\, b} \tag{1b}$$

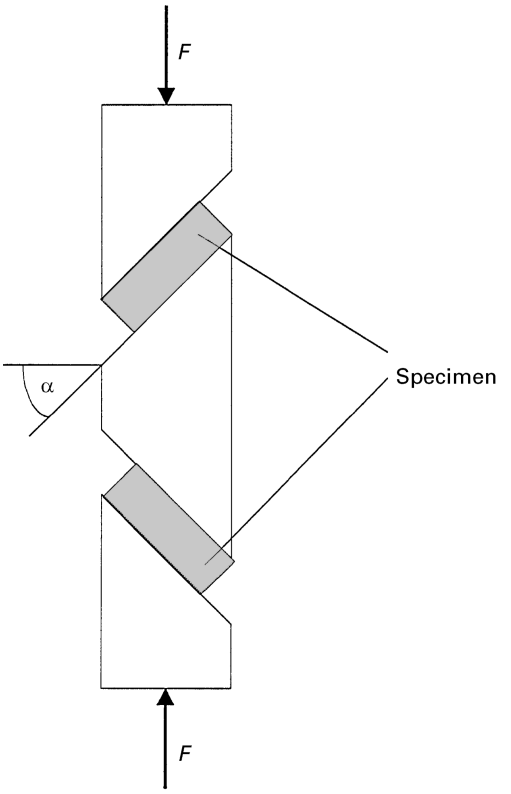


*Figure 2* Slant shear device. Specimen dimensions: $l = 12$ mm, $b = 6$ mm.

where τ is the shear stress, σ the compressive stress, $F$ the applied load, and $l = 12$ mm, $b = 6$ mm denote the specimen dimensions (see Fig. 2). Slant shear experiments were performed with three shear angles $\alpha = 63°$, 55° and 45°.

The specimens were accurately eroded to size and glued into the loading system using the UHU-Plus-Endfest 300 two-compound cementing material in a binding to hardening agent mixing ratio of 2:1. The slant shear test was not suited for application in high-temperature experiments because a high-temperature resistant cement is not available. Therefore, only untreated and heat-treated specimens were subjected to testing.

## 2.4. Crack propagation

Crack propagation was investigated on notched specimens in a four-point bending system using untreated specimens and specimens heat treated at 2060 °C. Flat notches with a ratio of notch depth to specimen height of 0.25 were induced into the specimens. The width of the notch was 50 μm. At the specimen level, an optical microscope was installed on an $X$–$Y$–$Z$ table at the loading system. The specimen was photographed at ×130 magnification near the notch bottom over the entire width, prior to loading. The specimens were loaded at a slow rate and, at the same time, crack opening or crack propagation was observed under the microscope. At characteristic loads the machine was stopped and the specimen photographed once more.

## 2.5. Equipment

Universal testing machines, supplied by Instron machines were available for the mechanical experiments. These machines were controlled in all experiments by a digital control system (M 8500). Data acquisition was via a PC which, by means of a GPIB interface and suitable data acquisition program, recorded the experimental data as path, load, deflection and time values.

Thermal treatment was made in vacuum using an UTS-350 vacuum furnace supplied by Balzers. The specimens were heated with a ramp of $1000\,^{\circ}C\,h^{-1}$ to $2060\,^{\circ}C$. The temperature was maintained over 5 h. Then the specimens were cooled down to room temperature. They will be called "heat treated" here.

For mechanical studies up to $1400\,^{\circ}C$, a high-vacuum furnace was built which surrounded the test equipment. The specimens were heated in vacuum at $1000\,^{\circ}C\,h^{-1}$ heating rate. Following 1 h holding time, the mechanical experiment was started.

The structure was evaluated under an optical microscope. General and detailed photographs of the structure, at $\times 50$ and $\times 200$ magnifications, were made.

In the scanning electron microscopic studies, a type SEM 505 microscope, supplied by Philips, was used. To be able to assess the fracture behaviour, pictures were made of the fracture surface. General views of the whole specimen surface were made in a $\times 40$ enlargement at an angle of inclination of the specimen of 45°.

## 3. Results

### 3.1. Untreated specimens

The stress–strain diagram of an untreated specimen has been represented in Fig. 3. It can be divided into three ranges: a linear initial range, a curved central range, and a linear range extending until shortly before specimen fracture. The fracture is spontaneous. A mean value of $107 \pm 6$ MPa is obtained for the strength. The Young's modulus at the beginning of loading is 67 GPa and in the second linear range about 38 GPa

In loading and unloading experiments, the maximum load was increased in each new cycle. A loading/unloading diagram is plotted in Fig. 3. After small loads have been applied, an irreversible deformation of the specimen during the course of unloading can be observed. The deformation behaviour depends solely on the respective maximum load and not on the history of the specimen. The maximum values of stress and strain almost coincide with the σ–ε diagram of monotonic loading. In the case where the specimen was loaded until shortly before fracture stress was attained, the irreversible deformation was about 0.31‰. The hysteresis loops are narrow. They are displaced in parallel with the amount of load applied and slightly widened. Shortly before specimen fracture, the hysteresis loops become tilted over. Only after fracture does the area inscribed by the hysteresis increase markedly. Each loading curve takes a linear course until the maximum value of the preceding hysteresis plot is attained.

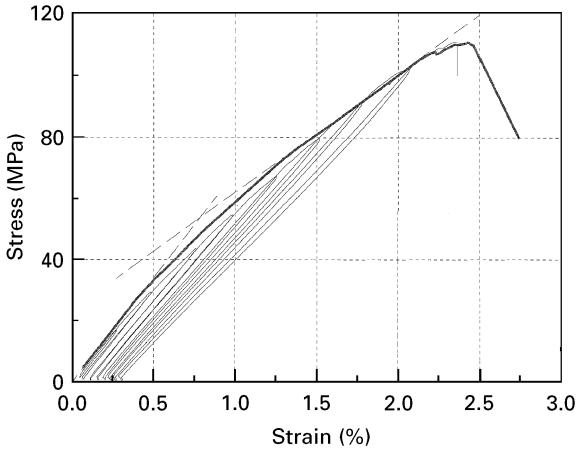


*Figure 3* Stress–strain diagram and loading/unloading diagram of an untreated specimen; four-point bending. (——) Monotonic loading, (——) loading/unloading, (— — —) linear range.

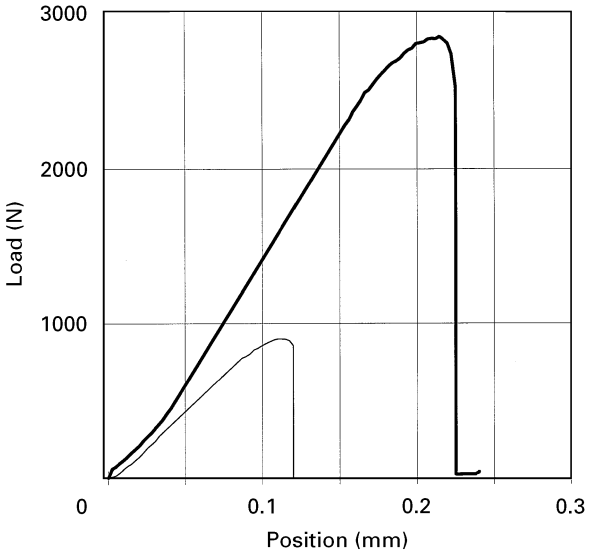


*Figure 4* Load–position diagram of (——) an untreated specimen and (——) a heat-treated specimen; slant shear test.

Fig. 4 shows the characteristic load–displacement curve of a specimen sheared at an angle of 63° in the slant-shear test. The plot is initially curved and then adopts a clearly linear course at about 20% of the maximum load. This range, marked by 75% of the fracture load, is followed by a non-linear range with slowly decreasing slope. The specimens undergo brittle failure.

The shear stresses and the compressive stresses superimposed on them are calculated using the maximum stress and the specimen dimensions. A shear stress and a compressive stress, as represented in Fig. 5 are obtained for each angle of loading of the slant shear device. Kadotani *et al.* [22] proposed that a linear relation exists between the shear stress and the compressive stress. The shear strength at zero compressive stress can be determined by extrapolation. A shear strength of about 25 MPa was obtained. The interlaminar shear strength must be higher than the extrapolated shear strength,

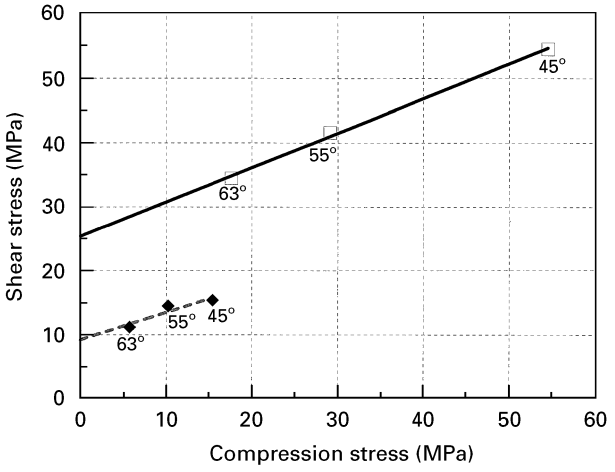


*Figure 5* Compressive stress versus shear stress for different angles of loading; slant shear test: (—□—) as received, (– –◆– –) heat-treated.

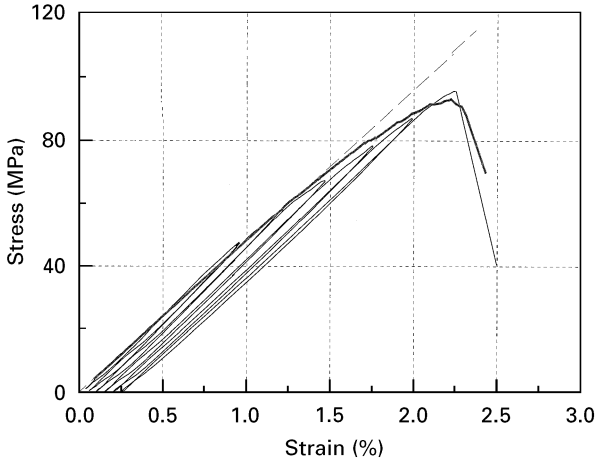


*Figure 6* Stress–strain diagram and loading/unloading diagram for a heat-treated specimen; four-point bending. (———) Monotonic loading, (——) loading/unloading, (— — —) linear range.

because the fracture plane is not between the fibre layers.

## 3.2. Heat-treated specimens

Specimens heat treated at 2060 °C are characterized by a linear stress–strain diagram up to about 70% of fracture stress (see Fig. 6). This is followed by a non-linear range extending up to fracture of the specimen. A mean value of 92 ± 3 MPa of bending strength was measured. It drops by approximately 30% compared to the untreated specimens. Fracture strain is comparable to that of untreated specimens and attains about 2‰. The Young's modulus at the beginning of loading is 46 GPa.

The loading/unloading diagrams of the heat-treated specimens are similar to those of the untreated specimens (see Fig. 6). The hysteresis loops have a sharp tip and are slightly tilted over before specimen fracture. The σ–ε diagram of the monotonically loaded specimen touches the points of return of the loading/unloading diagram. Irreversible deformation shortly before specimen fracture is comparable to the irreversible deformation of untreated specimens at the same stress.

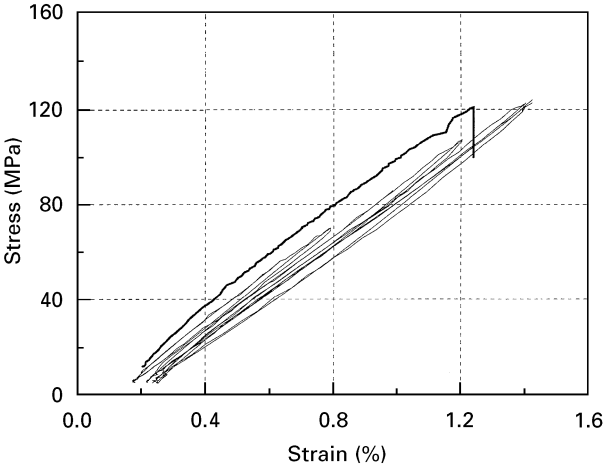


*Figure 7* Stress–strain diagram and loading/unloading diagram plotted at 1200 °C; four-point bending. (———) Monotonic loading, (——) loading/unloading.

In the slant shear test, the diagram is similar to that of untreated specimens (see Fig. 4). The interlaminar shear strength has been determined according to Kadotani *et al.* [22] (see Fig. 5). It is approximately 9 MPa. The decrease of shear strength for heat-treated specimens is about 67%.

## 3.3 High-temperature experiments

At 1200 °C, the three ranges of the σ–ε plot develop which had already been observed in experiments conducted at room temperature. The higher Young's modulus at the beginning of loading of the high-temperature specimens is clearly visible (Fig. 7). The Young's modulus increases, compared to room temperature, to 103 GPa at 1200 °C and attains 130 GPa at 1400 °C. The stress–strain diagram is linear from 35 MPa up to about 90% of fracture stress. Elongation at fracture diminishes. In the temperature range between 20 and 1000 °C the strength increases slightly with the temperature. The maximum of strength occurs at 1200 °C. A test temperature of 1400 °C produces a slight decrease in strength. This temperature is close to the melting point of elemental silicon of 1420 °C.

Fig. 7 shows a loading/unloading experiment conducted at 1200 °C. The envelope is a σ–ε diagram of a monotonically loaded specimen. Two features are different from the deformation behaviour of non-treated and heat-treated specimens, tested at room temperature: irreversible deformation up to fracture of the specimen is smaller at elevated temperatures than at room temperature. It is about 0.17‰ at the moment of specimen fracture. The plot of monotonic loading is much steeper than the loading/unloading plot and the cuspidal points no longer touch the monotonic curve.

# 4. Microstructural investigations

## 4.1. Structure

The structure of an untreated specimen was reported in Section 2.1.

High-temperature treatment causes changes in the composition of the specimens. At a temperature of 1500 °C and above, elemental silicon evaporates. The loss in weight amounts to approximately 6 wt %. Coarse crystalline SiC grains start growing in the direction of the fibre and the fine crystalline SiC is converted into coarse crystalline SiC. After thermal treatment at 1600 °C for 0.5 h, elemental silicon is no longer detectable on the specimen surface. Temperatures of 2060 °C maintained over 5 h cause complete reaction of silicon-containing fractions into coarse crystalline SiC. This process gives rise to cracks on the interphase between coarse and fine crystalline SiC.

## 4.2. Untreated specimens, SEM

Fig. 8 shows the development of a crack in a lateral view of a four-point bending specimen. In the untreated, specimen, only one through-the-thickness crack can be detected on the surface. It runs on a relatively straight path through the specimen. In 90° plies it passes primarily through shrinkage cracks.

The fracture surface is shown in Fig. 9. The fractures runs through shrinkage cracks in 90° bundles. This can be observed in the fibre bundles laid bare. Likewise, some protruding fibres can be recognized. These fibres bridge the shrinking cracks and fracture at small loading. Pores in the SiC matrix which would appear as a surface covered with crystallites, are hardly visible on the fracture surface. 0° bundles fail in sub-bundles. The number of steps corresponds to the number of shrinkage cracks per fibre bundle. The maximum fibre bundle pull-out is about 300 μm. The SiC matrix surrounding each fibre bundle is visible between the individual 0° bundles with a smooth fracture surface. Virtually no single-filament pull-out occurs. At the outer fibre, i.e. at maximum stress, failure is observed always in the gusset zones, i.e. at the points of maximum bending.


*Figure 8* Scanning electron micrograph, showing crack propagation in an untreated specimen; four-point bending.

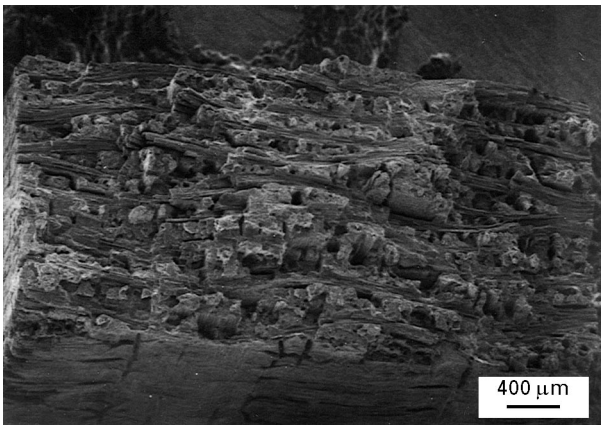


*Figure 9* Scanning electron micrograph of the fracture area of an untreated specimen; four-point bending.

The fracture surface of a specimen which failed in the loading/unloading test cannot be distinguished from the fracture area of a specimen which has been broken under monotonic loading.

The fracture surfaces of the slant shear specimens are identical for all angles of loading. The fracture is not parallel to any layer. It is either diagonal through the specimen through several plies of fibres, or occurs in a zigzag way so that the same ply is passed repeatedly. No defined course of fracture can be indicated.

## 4.3. Heat-treated specimens, SEM

Fig. 10 shows a lateral view of a specimen heat treated at 2060 °C following monotonic loading in the four-point bending test. The fracture occurred primarily between the SiC matrix and the fibre bundles. On 0° plies, the crack is often deviated and may penetrate into the next 0° ply on a laterally displaced path only.

The fatal crack increasingly passes through the SiC matrix between the 90° ply, but also through the shrinkage cracks and along the border of 90° fibre bundles, respectively.

The fracture surface of a specimen which has failed in the loading/unloading test cannot be distinguished

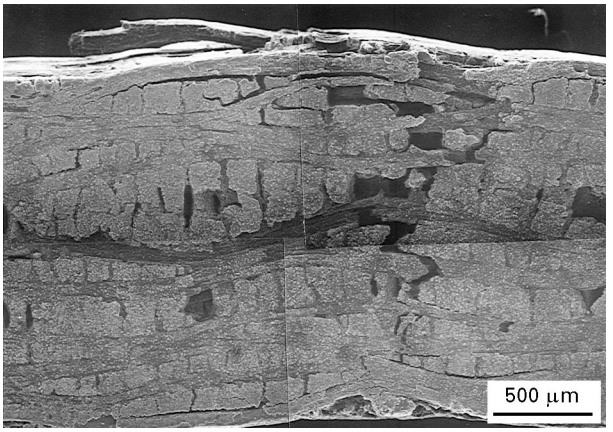


*Figure 10* Scanning electron micrograph, showing crack propagation in a heat-treated specimen; four-point bending.

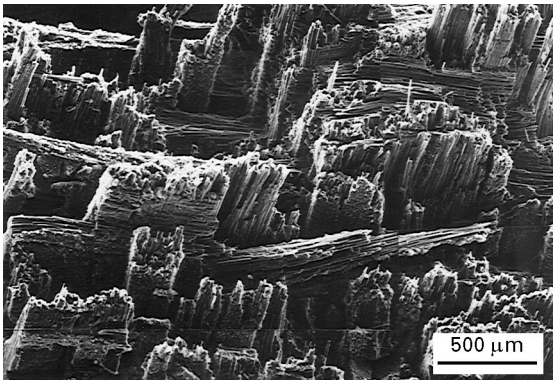


*Figure 11* Scanning electron micrograph of the fracture area of a heat-treated specimen; four-point bending.

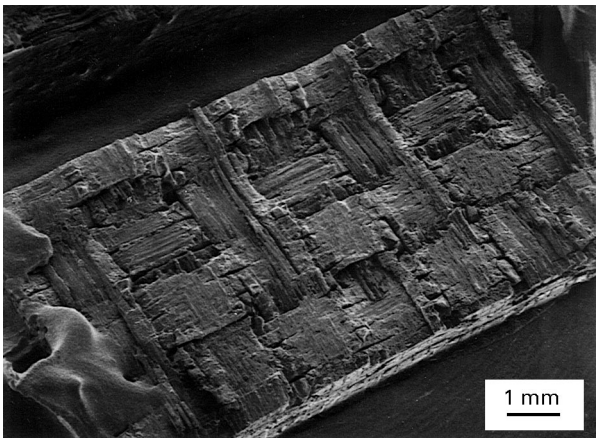


*Figure 12* Scanning electron micrograph of the fracture area of a heat-treated specimen; slant shear.

from the fracture area of a specimen ruptured under monotonic load, Fig. 11.

The fracture surfaces of heat-treated specimens which have failed in the slant shear test, run primarily along the matrix, parallel to the fibre ply. Hardly any fibre bundles cut in the normal direction are visible. This is shown in Fig. 12. Silicon carbide zones have been detected on the surface. The grain size is 5–10 μm.

### 4.4. High-temperature tests, SEM

Experiments conducted at elevated temperatures change the topography of the fracture surface of the specimens. In 90° bundles the crack runs predominantly through the SiC matrix, similar to heat-treated specimens. The pull-out of 0° plies is small, similar to that in specimens loaded at room temperature. The sub-bundles in the 0° fibre bundles have broken in two or three steps. Higher magnifications of a fibre bundle after fracture make visible both fibres debonded from the matrix and those permanently connected to the carbon matrix.

The fracture surface of a specimen which has failed in the loading/unloading test cannot be distinguished from the fracture surface of a specimen ruptured under monotonic load.

### 4.5. Crack propagation

The crack pattern of a notched unloaded specimen cannot be distinguished from that of a specimen loaded with 65% of the fracture load and that of a specimen loaded with 80% of the fracture load. If the force exceeds 90% of the fracture load, shrinkage cracks open near the bottom of the notch. Cracks run from the bottom of the notch into the fibres of the first 0° bundle below the bottom of the notch. If the load is increased further, the shrinkage cracks also widen below the second and third 0° bundles. The cracks become longer and run into the SiC matrix of the 0° fibre plies. It has not been clarified whether cracks propagate only in the SiC matrix surrounding the 0° fiber bundle, or whether fibres running in the direction of loading have also been cut. Finally, the specimen fails spontaneously by failure of the fibre bundle in the direction of loading.

In heat-treated specimens, crack propagation in the SiC matrix was observed from approximately 80% of the maximum load onwards. The fibre bundle above the crack in the direction of the higher tensile loading does not yet indicate any damage. From about 90% of fracture loading onwards, the cracks run into the 0° fibre plies. The specimens fail spontaneously by failure of the fibre bundles of the 0° fibre plies.

## 5. Discussion

### 5.1. Material

The experimental findings can be described with a two-component material model. The first component is the fibre bundles in the direction of loading. It consists of carbon fibres and the matrix embedded in them. The matrix consists mostly of carbon. The shrinking cracks in the fibre bundles divide the latter into sub-bundles.

The second component is made up of the rest of the structure which consists of the fibre bundles normal to the direction of loading and the SiC matrix. The components are chemically bound.

An attempt will now be made to explain, in qualitative terms, the observed mechanical behaviour using a two-component model where cracks are embedded in component 2. This is represented schematically in Fig. 13.

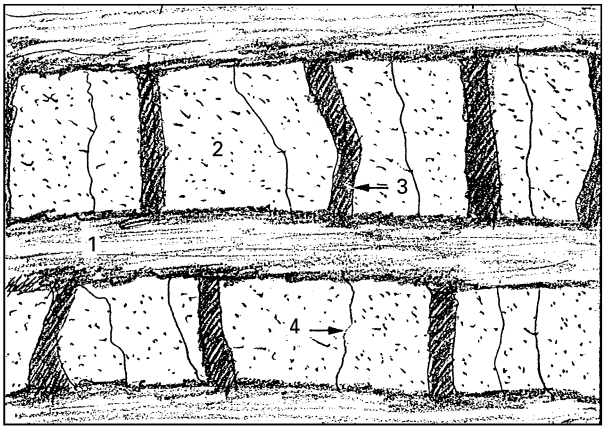


*Figure 13* The two-component model for microstructure; (1) 0° plies, (2) 90° plies, (3) SiC matrix, (4) shrinkage crack.

## 5.2. Untreated specimen

The stress–strain diagram of the untreated specimen (see Fig. 3) can be divided into three ranges. In the first and third ranges the stress–strain diagram takes a linear course, in the second range it is curved.

In the first linear range, the stress is distributed among the two components according to the rule of mixing. The behaviour is linear-elastic, as known from other composites [2–4].

In the non-linear range, the stress exceeds a critical value in the second component. Fibres running normal to the direction of load and bridging the shrinkage cracks will rupture. In the second component, through-the-thickness crack paths develop. In the case of further increase in loading, the stress in the second component exceeds the critical value at yet more points. Additional 90° fibres break. This process is comparable to the onset of progressive matrix damage, as described in the literature, which, likewise, starts from a given load onwards [4, 5]. At the load at which this damaging process is completed, the stress–strain diagram reaches the second linear range.

In the second linear range the increase in load does not produce additional damage to the second component. The stress is accommodated mainly by the fibre plies in the direction of loading which are deformed elastically. From 90% of the fracture load onwards, the stress–strain curve becomes markedly non-linear. Shrinkage cracks and cracks in the SiC matrix open and extend. If the load is increased but slightly, the specimen fails spontaneously by failure of the fibre bundles in the direction of loading. No crack bridging of 0° bundles occurs. In analogy with the literature [6], failure of the specimen is caused by failure of the fibre sub-bundle in the direction of loading. The failure of individual fibre bundles preceding material failure, as observed by Rouby and Reynaud [4], has not been observed in our work. The fibre bundles fail due to concentration of stresses in the gusset zone of the cross-plies.

In the loading/unloading experiments, an irreversible deformation of the specimen was already observable at small loads. The fibre bundles in the direction of loading do not always run parallel to the load because of the structure of the fabric. When subjected to load, the fibre bundles tend to straighten out and are strained. Straining of the fibres is a reversible process, whereas straightening of fibres in the direction of loading is irreversible.

The following mechanisms may account for irreversible deformation. The crack structure and the pores allow the fibres to move and to straighten out. Friction between the two material constituents, as well as geometric misfit, prevent the fibre bundles from returning into their original positions. Friction in the C/SiC material investigated is obviously higher than in the material examined by Bouquet *et al.* [2] who observed irreversible deformations at higher loads only. Unlike in the SiC/SiC material [2], matrix fragments are not responsible for irreversible deformation.

The value pairs of maximum stress and strain fall on the curve of the stress–strain diagram which is obtained under monotonic loading. This suggests that the amount of damage in the specimen is determined by the highest stress applied to the specimen.

## 5.3. Heat-treated specimen

The stress–strain plot of the specimen heat treated at 2060 °C takes a linear course up to ~60% fracture stress. It kinks shortly before specimen fracture. Following heat treatment, the bending strength of a specimen heat treated at 2060 °C diminishes by about 30%. The Young's modulus at the beginning of loading is much lower than the Young's modulus of an untreated specimen.

Heat treatment causes the coarse-grained SiC crystallites to grow at the expense of the fine-grained crystallites. Crack paths through the thickness develop in the SiC matrix between fine-grained and coarse-grained crystallites, and the pores. This is particularly visible in the SiC layer between the individual plies which is heavily reduced in strength due to recrystallization. This is the reason why the second material component is hardly capable of accommodating any additional stress. Under loading the total stress is accommodated by the fibre bundles in the bundles in the direction of loading. This leads to a decline in Young's modulus, compared to an untreated specimen and to a linear stress–strain curve until 70% of the fracture stress is attained.

In the non-linear range, crack propagation in the SiC matrix was observed at 80% of the maximum stress and hence more pronounced deformation of the specimen occurs. Moreover, the first damage caused by shear stress can be noticed which is due to the different elastic properties of the fibre, carbon matrix and SiC interphase. Observation of the lateral faces yielded strong crack propagation along 0° plies. First the recrystallized SiC layer between the plies fails. At suitable defect sites, the crack can then propagate into the 0° bundle underneath. The missing stress transfer is reflected by a strong kink in the $\sigma$–$\varepsilon$ plot. Failure of the specimen is determined by the fibre sub-bundles in the direction of loading.

The loading/unloading behaviour is analogous to that of untreated specimens.

The shear strength was greatly diminished by thermal treatment. Delamination cracks become visible, these have also been described elsewhere [11].

## 5.4. Failure behaviour at high temperature

The Young's modulus of the specimen increases at elevated temperatures, as also described by Mahfuz *et al.* [10]. One of the reason is the higher densities of the anisotropic carbon fibres at elevated temperature. The other reason is that the fibres are woven. If the specimen is heated, the woven structure causes compression of the bundles within a macroscopically visible loop. Now, more material contributes fractions to the load transfer than at room temperature. Tests made at room temperature produced a $\sigma$–$\varepsilon$ plot resembling the maximum values of a loading/unloading diagram. This was not the case at high temperatures. The fibres in the direction of loading do not change

their behaviour as a whole. Therefore, the rest of the structure must be responsible for the change in mechanical behaviour. It has not yet been clarified which mechanism accounts for the lower Young's modulus in loading/unloading experiments. However, the effect we observed may not be as conclusive as it might seem at first sight, because there is a considerable amount of scatter in the material properties.

## 6. Conclusion

The mechanical behaviour of a C/SiC material, infiltrated by liquid siliconization, was studied. Microstructural properties were attributed to the observed failure behaviour. The material can be described in terms of a two-component model with component one denoting the fibres bundles in the loading direction and component two summarizing the rest of the microstructure. The fibres in the loading direction are responsible for the deformation and the fracture behaviour, whereas the damage mechanisms depend on the rest of the microstructure. High-temperature loading up to 1400 °C does not change the microstructure, but slightly influences the deformation behaviour. If the material is heat treated at very high temperatures (2060 °C), the microstructure is changed. This leads to a reduction of the strength and of the interlaminar shear strength.

## References


1. R. KOCHENDÖRFER, in "Faserkeramik für heiße Reentry-Strukturen", Proceedings of Techkeram '89, Wiesbaden 1989.
2. M. BOUQUET, J. M. BIRBIS and J. M. QUENISSET, *Compos. Sci. Technol.* **37** (1990) 223.
3. A. G. EVANS, *J. Mater. Sci.* **29** (1994) 3857.
4. D. ROUBY and P. REYNAUD, in "6th European Conference on Composite Materials" edited by R. Naslain, J. Lamon and D. Doumengts, (Woodhead Publishing, Abingdon, 1993) pp. 499–513.
5. S. F. SHULER, J. W. HOLMES, X. WU, D. ROACH, *J. Amer. Ceram. Soc.* **76** (1993) 2327
6. E. INGHELS and J. LAMON, *J. Mater. Sci.* **26** (1991) 5403.
7. J. AVESTON, G. A. COOPER and A. KELLY, "Single and multiple fracture, the properties of fibre composites" (IPC Science and Technology Press, Guildford, 1971 pp. 15–26.
8. P. REYNAUD, doctoral thesis, INSA Lyon (1992).
9. K. M. PREWO, *J. Mater. Sci.* **24** (1989) 1373.
10. H. MAHFUZ, P. S. DAS and S. JEELANI, *ibid.* **28** (1993) 5880.
11. O. SBAIZERO, P. G. CHARALAMBIDES and A. G. EVANS, *J. Amer. Ceram. Soc.* **73** (1990) 1936.
12. A. G. EVANS and D. B. MARSHALL, *Acta Metall.* **37** (1989) 2567.
13. A. G. EVANS, J. M. DOMERGUE and E. VAGAGGINI, in "6th European Conference on Composite Materials" edited by R. Naslain, J. Lamon and D. Doumengts, (Woodhead Publishing, Abingdon, 1993) pp. 1–32.
14. D. S. BEYERLE, S. M. SPEARING and A. G. EVANS, *J. Amer. Ceram. Soc.* **75** (1992) 3321.
15. E. INGHELS and J. LAMON, *J. Mater. Sci.* **26** (1991) 5403.
16. Z. G. WANG, C. LAIRD and Z. HASHIN, *ibid.* **26** (1991) 4751.
17. D. DINKLER, A. FINK and B. KRÖPLIN, "Constitutive Laws for Fibre Reinforced Ceramics", Preprint of the Proceedings of the AIAA/DLRG, 5th International Aerospace Planes and Hypersonics Technologies Conference, report no. AIAA-93-5038, (1993).
18. Y. WANG, C.-Y. HUI and A. JAGOTA, *Mech. Mater.* **15** (1993) 183.
19. J. PLEITNER and H. KOSSIRA, in "6th European Conference on Composite Materials" edited by R. Naslain, J. Lamon and D. Doumengts, (Woodhead Publishing, Abingdon, 1993) pp. 565–72.
20. W. KRENKEL, in "Proceedings of the International Conference on Spacecraft Structures and Mechanical Testing", Nordwijk, 19–21 October 1988.
21. P. SCHANZ, "Faserkeramik durch Flüssigsilizierung", (Carl-Cranz-Gesellschaft Lehrgang BW 3.01, Stuttgart, 1992).
22. F. KADOTANI and F. AKI, Composites **15** (1) (1984) 57.



*Received 15 December 1995*
*and accepted 4 April 1996*